Heliyon 5 (2019) e02215

Contents lists available at ScienceDirect

Heliyon

journal homepage: www.heliyon.com

Synthesis and applications of $CaCO_3$/HPC core–shell composite subject to heavy metals adsorption processes

Mahmoud Fathy [a,*], Mohamed A. Zayed [b], Y.M. Moustafa [a]

[a] Egyptian Petroleum Research Institute (EPRI), AhmedEl-Zomer, Nasr City, Box. No. 11727, Cairo, Egypt
[b] Chemistry Department, Faculty of Science, Cairo University, Giza, 12613 Egypt

ARTICLE INFO

Keywords:
Engineering
Materials science
Chemistry
Environmental science
Adsorbent
Core-shell
Polystyrene
Porous carbon
Composite
Heavy metals

ABSTRACT

Core-shell particles are a class of materials from nanostructures that have received increased attention recently due to their interesting properties and wide range of applications in catalysis, biology, chemistry of materials and sensors. Simple and cost-effective one-pot synthesis route to directly prepare $CaCO_3$@highly porous carbon microsphere in a core–shell structure (denoted as $CaCO_3$/HPC) had been developed as a high-performance heavy metals sorbent. XRD (X-Ray Diffraction), SEM (scanning electron microscopy), Raman, FTIR (Fourier Transform Infrared Spectroscopy) and BET tools were used in structure characterization of the products. The adsorption properties of the products obtained were studied. From this study the adsorption performances of $CaCO_3$/HPCwere found to be optimal by comparing the maximum adsorption capacity of heavy metal ions (Pb (II) and Co(III)) with $CaCO_3$/HPC.The adsorption of $CaCO_3$/HPCtest to Pb(II) and Co(III), in particular Pb(II) had a good effect over a wide pH range (pH 2–7). The maximum adsorption capacitiesof $CaCO_3$/HPC for Pb (II) and Co(III) were 677.6 mg/g, and 308.5 mg/g, respectively, at pH = 6 (lead ion was 5.5) and 25 °C, and the adsorption rate was fast. The lead ions can be adsorbed almost entirely in 5 minutes and only 0.2 g/L was the best effective doseof adsorbent. The prepared and carefully testednanocomposites had been found to be of excellent performances in adsorption and in analytical regeneration. The adsorption processof Pb(II) and Co(III) through core shell of the preparednanocomposite adsorbent was found to be a second-order chemical adsorption and fit for Langmuir and Freundlich isotherms, in the form of amonomolecular and multi-layer heavy metal adsorptionprocesses. The ($CaCO_3$/HPC)-based sorbents (with and without) pelletization shows superior heavy metals adsorption performances compared to a $CaCO_3$-based sorbent.

1. Introduction

Core/shell structured organic/inorganic composite microspheres of various compositions have been attracted much attention, because of their enhanced properties including mechanical, chemical, electrical, rheological, magnetic, and optical. To date, these kinds of composite microspheres are mainly applied in the area of drug delivery, coatings, catalysis, colloidal crystals, and diagnostics and so on [1, 2].

Previous studies had beenestablished technology for water pollution controlby implementation of several techniques such as reverse osmosis (RO), electrochemical precipitation, ion exchange (IE) and adsorption. Nevertheless, there are some limitations of these techniques that need to be addressed for effective water remediation. Some drawbacks like high energy requirement, a large amount of sludge production and maintenance cost are considered a major challenge to handle [3]. For instance, the well-recognized precipitation technique based on economical approach produces a large amount of precipitate sludge that involves an additional process for the further treatment [4]. Meanwhile, RO technique is promising to be effective in reducing metal ions, but it requires high operational cost and limited pH range. IE is a convenient method to treat the heavy metal ions such as chromium, but not much studies have been conducted and also the technique is not cost-effective [5].

Nowadays, a broad variety of functionalized Ca-based materials are used to remove heavy metal ions byion exchange, sorption or chemical reactions [6]. Porous activated carbon water-soluble graphene may have superior graphene quality for heavy metal adsorption. The porous activated carbon surface is known to be easily modifiedto further changes in

* Corresponding author.
E-mail address: fathy8753@yahoo.com (M. Fathy).

https://doi.org/10.1016/j.heliyon.2019.e02215
Received 11 June 2019; Received in revised form 15 July 2019; Accepted 30 July 2019

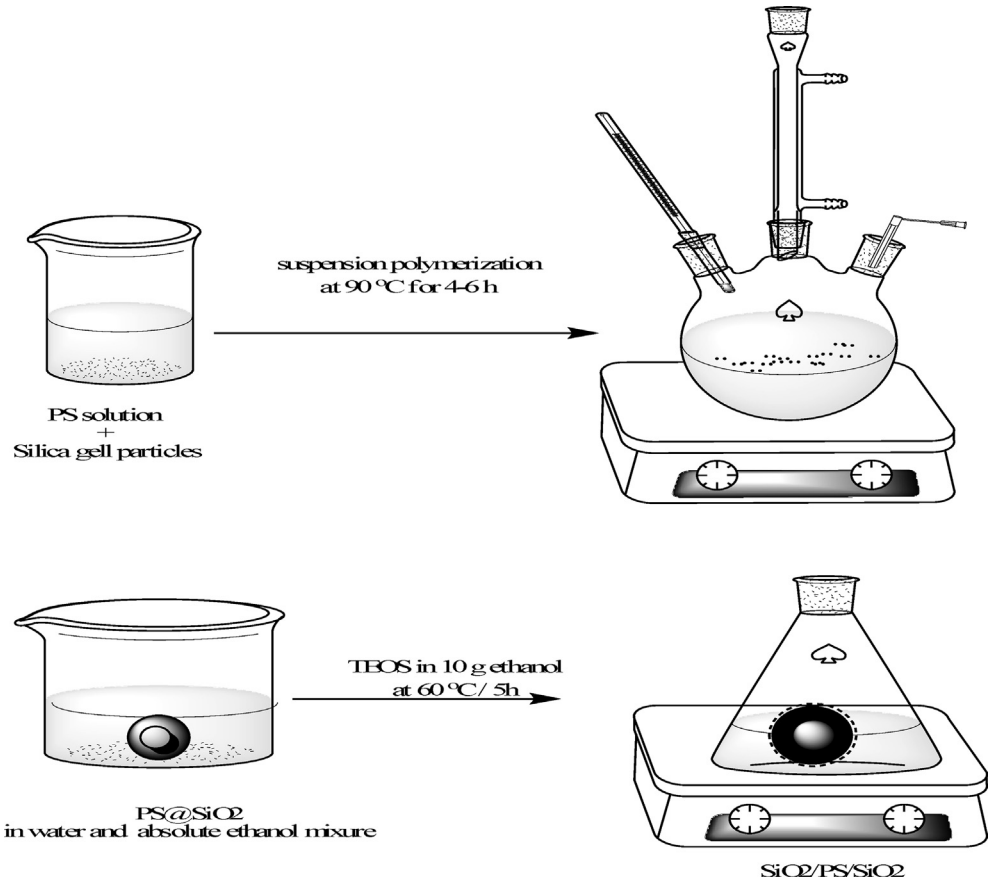

Scheme 1. Flow chart of preparation of porous SiO_2/PS/SiO_2core shell composite.

its characteristics. The safety of carbon-based nanomaterialswith all the promise benefits and potential, including nanotubes, graphene, and their derivatives, is comparatively little known. It is therefore necessary to minimize the persistence of core shell adsorbents in treated water based on Porous Activated Carbon (PAC). The removal of PAC from water, however, has demonstrated its own difficulties [7].

Mesoporous materials provide high surface areas, large pore volumes and tunable pore sizes for potential applications as absorbents, catalysts, chemical sensors, drug-delivery systems, and their presence in various electrochemical devices [8]. By proper tuning of the fabrication conditions, such as suitable reaction conditions and organic templates; it can be prepared to consist of mesoporous materials with high-flexibility in dimension, composition and morphology [9]. Mass production of mesoporous materials has become possible by using a cheap template and inorganic sources and operating under environmentally friendly reaction conditions. Several mesoporous materials/$CaCO_3$ composite sorbents have been reported [10].

Magneticmaterialor carbonate polymer is a new type of functional organic-inorganic composite that had been quickly created over the past few years. The magnetic structure of magnetic polymer components primarily consists of nickel, iron, cobalt and its alloys, π-Fe_2O_3, Fe_3O_4 and other iron oxides [11, 12].

Recently, polymers have received increasing attention in wastewater treatment because of their efficient removal of heavy metals, especially those polymeric hydrogels with cross-linked network structure and the functions of adsorption, water absorption, water retention, and slow of water release [12]. A low-cost adsorbent, aminated calcium lignosulfonate (ACLS) has been manufactured and effectively implemented to Congo red and Titan yellow color dyeadsorption [13, 14].

In particular, polystyrene (PS) microspheres have presented some major advantages when they are used as the polymeric cores, such as their facile synthesis, controllable monodisperse size and shape, various functional groups [15], and easy removal through high-temperature calcination or dissolution with an appropriate solvent [16, 17].

Many carbon salt composites such as carbon composite lignin-based adsorbent had been prepared with glucose as a carbon source, calcium lignosulfonate and triethylenetetramine as raw materials, respectively, using hydrothermal methods. By studying the addition of carbon and triethylenetetramine; the optimum requirements for synthesis were determined. The adsorbent was used to adsorb Congo red and Eriochrome black R azo dyes [14, 18].

In the present study, $CaCO_3$/HPC core shell composite was selected as the active sober for heavy metal adsorption. It provided a highly stable framework under severe temperature conditions. The effects of adsorption dose, solution pH, contact time, and temperature were investigated. Thermodynamic parameters, kinetic, equilibrium and adsorption isothermsof $CaCO_3$/HPC core shell composite were determined to analysis of the adsorption behavior.

2. Experimental

2.1. Materials

The $Ca(OH)_2$ (96%), HCl (37%), NH_4OH (28%), silica gel (50 mm) and tetraethoxyorthosilicate (TEOS, 98%) were purchased from Sigma-Aldrich Co. LTD and used without further purification. Waste polystyrene form foam national company. The CO_2 gas was purchased from Daedong Gas Technology Company.

2.2. Preparation of PS/SiO_2 composite organic core shell composite

The waste PS microspheres were prepared *via* the suspension

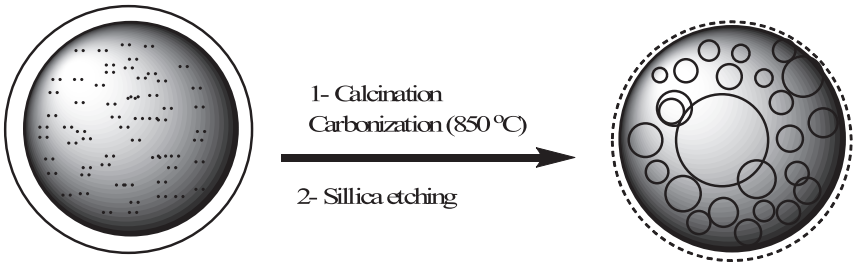

Scheme 2. Flow chart for preparation of porous HPC microsphere with empty core.

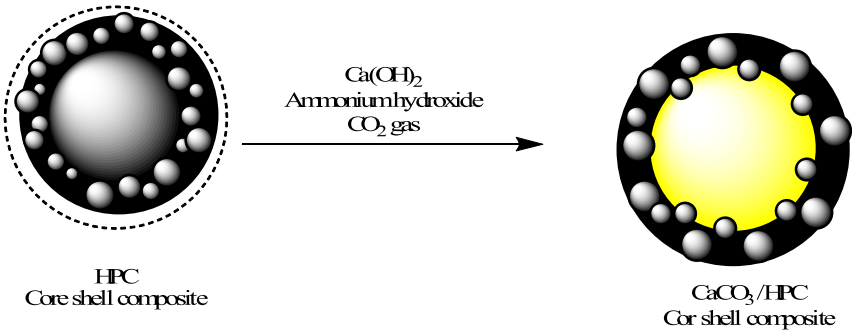

Scheme 3. low chart for preparation of $CaCO_3$/HPC core shell composite.

polymerization method.

In short, polystyrene (20 g) and 10 g silica gel (50 mm) dissolved in 50 ml chloroform then the solution added to 250 g water was loaded into a 500 mL round-bottom flask fitted with a magnetic stirrer, a temperature controller thermometer.

Then the above mixture was deoxygenated by bubbling nitrogen gas at room temperature for 30 min and heated to 60 °C under constant stirring. The reaction was allowed to proceed for6 h at 90 °C, and then cooled to room temperature. Finally, the PS microspheres were obtained.

The coating reaction was carried out *via* the hydrolysis and condensation of TEOS, and yielded amorphous silica at alkaline aqueous media in the presence of PS@Silica gel beds, respectively. A typical process to prepare silica-coated PS@Silicaspherical was described as follows: 5 g of the as-obtained PS@Silicadispersion was diluted with 10 g of water and 40 g of absolute ethanol. The colloid dispersion was adjusted to pH = 8 by NH_4OH solution. Then, the reaction mixture was slowly heated to 60 °C, followed by slow addition (5 g/h) of the mixed solution (3 g TEOS in 10 g ethanol). The reaction mixture was stirred for 5 h under constant magnetic stirring. After that, the reacting mixture cooled to room temperature, filtered and the precipitate washed several times and dried overnight. Finally, the core/shell structureof the composite microspheres was obtained under alkaline condition and denoted as composite- SiO_2/PS/SiO_2. The preparation process of the composite obtained followed the following Scheme 1.

2.3. Carbonization of organic core shell composite resins

The prepared porous SiO_2/PS/SiO_2core shell composite was carbonized at 900 °C for 3 h in N_2 flow with a heating rate of 2 °C min^{-1}, thus obtaining the HPC. The carbonization yield was measured to be 60%. The obtained blank sample without –CO– Crosslinking bridges and its carbonized product were denoted as HPC (high porous carbon) microsphere. **Carbonization of the organic core shell composite resin to obtain HPC followed** Scheme 2**.**

2.4. Preparation of $CaCO_3$/porous carbon core shell composite

Approximately 4.198 g of $Ca(OH)_2$ was mixed with 200 ml of deionized water. To completely dissolve the $Ca(OH)_2$ hydrochloric acid was added until the turbid solution became transparent. The stock solution (15 ml) was charged to a round bottom flask with a stirring bar [19]. Ammonium hydroxide solution acting as a catalyst was slowly added to the round bottom flask with stirring. Through the tube and needle, the CO_2 gas was added to the round bottom flask with various times at ambient condition. The synthesized $CaCO_3$–HPC composite (Scheme 3)was separated and washed with methanol several times.

2.5. Adsorption studies

The experiments of adsorption were performed in a series of flasks containing 100 mL solutions of metal ions at desired concentration and mass of adsorbent herbs. The mixtures were shaken for 16 h at 120 rpm using a shaker ("Rotaterm" Orbital and linear shaker). The mixtures were filtered, and determined the concentrations of heavy metals by inductively coupled plasma (ICP) mass spectrometry. The effect of adsorbent doses from 0.1 to 1.5 g on the metal adsorption was studied. The initial concentration used was 250 mg/L. The effect of pH on the process of heavy metal adsorption was investigated at pH values from 3 to 12, adjusted either with 1 M HCl or 1 M NaOH using a pH meter, to monitor the pH change. In addition, the contact time was varied between 1 and 2 h. The effect of temperature was studied from 25° to 65 °C for 2 h using 0.5 g of the adsorbent at an initial metal concentration of 250 mg/L. The adsorption equilibrium was investigated for different metal concentrations between 100 and 700 mg/L. In addition, kinetics experiments were conducted with 100 mg/L metal and 0.5 g of adsorbent at room temperature with stirring at 120 rpm for 2.5 h.

At equilibrium, the adsorption, q_e (mg/g), was calculated by Eq. (1):

$$qe=(C0-Ce)Vm \quad (1)$$

where C_0 and C_e (mg/L) are the concentrations of heavy metals at initially and at equilibrium, respectively. V is the solution volume (L) and m is the dry adsorbent mass (g).

The heavy metal adsorption percentage (Ads_{HM} %) from the solution was calculated as follows Eq. (2):

$$AdsHM\%=(C0-Ce)C0\times100 \quad (2)$$

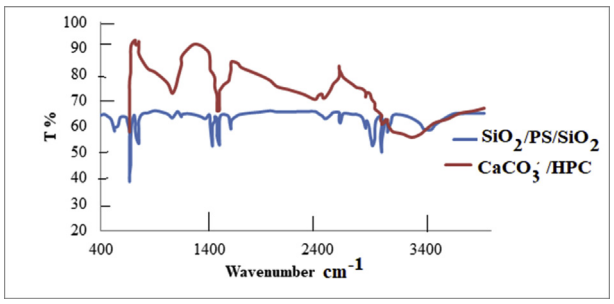

Fig. 1. FTIR spectra of SiO_2/PS/SiO_2 and $CaCO_3$/HPC core shell composites.

For describing the adsorbent behavior, the pseudo first and second order adsorption Kinetic models were applied.

The equilibrium data were then fitted using the Langmuir and Freundlich isotherm models.

The thermodynamic parameters, including the changes in enthalpy (ΔH°), entropy (ΔS°) and free energy (ΔG°), were calculated to describe the adsorption process onto *composite*.

2.6. Characterization

The morphologies and element composition were investigated using a Philips XL30 SEM field scanning electron microscopy (SEM) system. The thermal stability of the particles and mass percent of the sorbent were measured by using thermogravimetric analysis (TGA) (TA instrument Q50, USA) carried out from 25 to 800 °C at a heating rate of 5 °C/min. The surface area and pore volume were determined with a N_2 adsorption-desorption isotherm measured at 77 K by using a physisorption analyzer (Micromeritics, Model ASAP 2020, USA) determined by Brunauer-Emmett-Teller (BET) method and t-plot method. The pore size distribution and pore volume were derived from the adsorption branch of isotherm by using the Density-Functional-Theory (DFT) model. Infrared spectra of porous carbons were recorded on an FT-IR spectroscopy (VERTEX. 70 Fourier transform infrared spectrometer, Bruker, USA).

3. Results and discussion

3.1. FTIR analysis

Regarding the organic core shell composite SiO_2/PS/SiO_2, the major peak of SiO_2 absorption is 1100 cm^{-1} as shown in Fig. 1. It revealed several characteristic peaks of pure PS. The absorption peaks were attributed to the aromatic C–H stretching vibration at 3026 and 2920 cm^{-1}. The peaks at 1492, 1452, 754 and 698 cm^{-1} are associated with aromatic C–C stretching, C= C bond stretching mode of the benzenoid ring, out - of-plane bending of aromatic C–H and out - of-plane bending of the 1,4 replaced benzene ring, respectively [20, 21].

In the present work, FT-IR is employed to analyze the surface groups of $CaCO_3$/HPC core shell composite after surface modification. A broad band at around 3343 cm^{-1} is observed in both samples. It is mainly caused by the O–H stretching vibration of the adsorbed water molecules and the –OH radical on the surface of $CaCO_3$/HPC core shell composite [22], which also has a weak bending vibration mode corresponding to the band recorded at 1618 cm^{-1}due to the introduced oxygen-containing groups after surface modification and oxidation. The weak band at 1732 cm^{-1} denote the absorption of the C-O stretching vibration of a –COOH radical. These surface functional groups play important roles in improving the hydrophilicity of the carbon surface, and are essential for increasing the specific capacitance of $CaCO_3$/HPC core shell composite. The synthesized $CaCO_3$/HPC core sell nanocomposite dispersed in methanol was dropped to KBr plate and dried for FTIR spectra, which was achieved $CaCO_3$ characteristic absorption peaks at 1450, 875, and 712 cm^{-1} as shown in Fig. 1. The major absorption peak corresponding to 1450 $cm^{-1}$for pure $CaCO_3$ is appeared at 1480 cm^{-1}. The sharp absorption peaks of $CaCO_3$ were appeared at 850 and 750 cm^{-1}, which are slightly higher energy than pure $CaCO_3$ absorption peaks. The 5 min bubbling of CO_2 shows relatively stronger absorption peaks for $CaCO_3$ and SiO_2compared with 3 min bubbled sample.

3.2. SEM analysis

Fig. 2 shows the surface morphologies of the all core shell composites sorbent before and after the addition of $CaCO_3$ core.

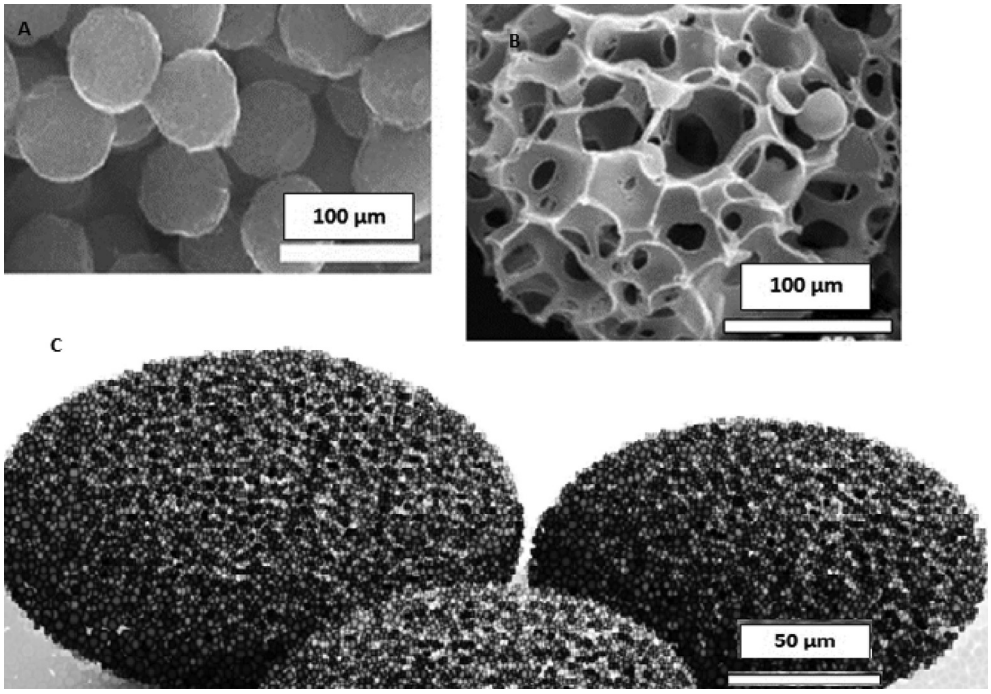

Fig. 2. SEM of a) SiO_2/PS/SiO_2, b) HPC and C) $CaCO_3$/HPC core shell composites.

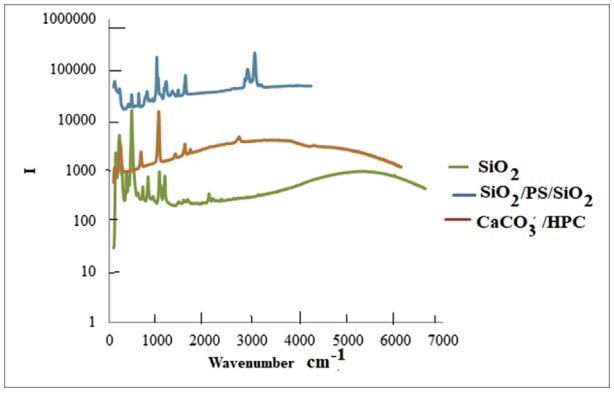

Fig. 3. Raman spectra of SiO_2, $SiO_2/PS/SiO_2$ and $CaCO_3$/HPC core shell composite.

With respect to $SiO_2/PS/SiO_2$ organic core shell composite; Fig. 2 shows the particle shapes and diameters which have small particles with several 100–200 μm. Also we can say that the appearance of the surface morphology of both the $CaCO_3$-based sorbent and the $SiO_2/PS/SiO_2$-based found to have isolated particles. The $CaCO_3$-based sorbent consisted of dispersed particles of about 200μm and we can see that the particle size became a little bit larger. This increase depends on the decrease of the surface area and porosity caused by the growth and fusion of particles. This sorbent seemed to cause fusion within the sample so that the sintering between mutual particles was slightly less than that of the $CaCO_3$-based sorbent. Therefore, $CaCO_3$/HPC composite can be used as a stable framework structure and diffusion barrier to improve the stable structure and adsorption process.

3.3. Raman analysis

Fig. 3 shows the Raman spectra of SiO_2, $SiO_2/PS/SiO_2$ and $CaCO_3$/HPC core shell composite revealing the superposition between the lines due to the polymeric matrix (PS) and the filler $CaCO_3$ in the $CaCO_3$/HPC core shell composite [23]. The crystalline SiO_2 could come from the remaining unreacted quartz dust during the industrial production process [24]. In the study, the 1080 cm^{-1} peak was attributed to the symmetrical stretching (SS) of the Si-O tetrahedral, the 700 cm^{-1} to the Si-O-Si symmetrical bending and deformation of Ca-O. The peak at 465 cm^{-1} was assigned to the internal deformations of Si-O tetrahedral the O-Si-O linkage and the 280 cm^{-1} to Ca-O bond [25]. Designation of these peaks are supported by work done by Leeman on alkali-silica reactions as well as Raman studies on silicates [26]. Fig. 1 shows that the Raman lines of the $CaCO_3$/HPC are rapidly broadened and weaker comparing with the $SiO_2/PS/SiO_2$ core shell composite, a behavior observed in other polymer-carbon nanotube composites and assigned [27] to the dephasing of the local motions of macromolecular chains due to the interactions with the HPC. The left panel of Fig. 1 shows a micrograph of the as obtained $CaCO_3$/HPC containing a large fraction of HPC carbon structure. It is noticed that the HPC are thin and very uniform. In contrast with this result, the PS with SiO_2 core shell composite are thicker and exhibits large and numerous beads [28]. The results of Raman mapping indicate the effectiveness of modification of the entire $CaCO_3$filler surface. The results show that the HPC layer is present in modified $CaCO_3$/HPC composite; in turn on surface of modified silica it is evenly distributed. Moreover, there are no visible the places with higher amount of aromatic groups. Even distribution of the aryl layer and therefore of the hydroxyl groups is very important due to the uniform effect of the $CaCO_3$ filler on the properties of the composite at its entire volume [28].

3.4. Crystallinity analysis

Fig. 4 shows XRD curves of SiO_2, $SiO_2/PS/SiO_2$ and $CaCO_3$/HPC composites.

As can be seen from Fig. 4, $SiO_2$and $SiO_2/PS/SiO_2$had a strong 2θ peak at 21.6° and 26.1°, which was the characteristic peak of V-type crystal formed during thermo-mechanical processing. $CaCO_3$/HPC had a strong 2θ peak at 22.7°, which was the 002 crystal diffraction peak of HPC, a sharp and strong 2θ peak at 31.2°, which was the typical peak of $CaCO_3$, confirming the composite of $CaCO_3$/HPC core shell composite [29, 30, 31, 32]. We can see that the precipitated crystal $CaCO_3$/HPC contained calcite crystals and some of those contained vaterite crystals. It is generally known that vaterite is less stable and has a higher solubility than calcite, thus the vaterite can be easily dissolved and then precipitated into the most thermodynamically stable calcite crystals via the solvent-mediated mechanism [33]. Additionally, the characteristic peak of $CaCO_3{\cdot}6H_2O$ could no longer be observed, and it was difficult to clearly observe the characteristic peak of amorphous calcium carbonate due to the development of calcite (Fig. 4). In contrast, the characteristic peak of the (104) crystal face of calcite became well developed. Although

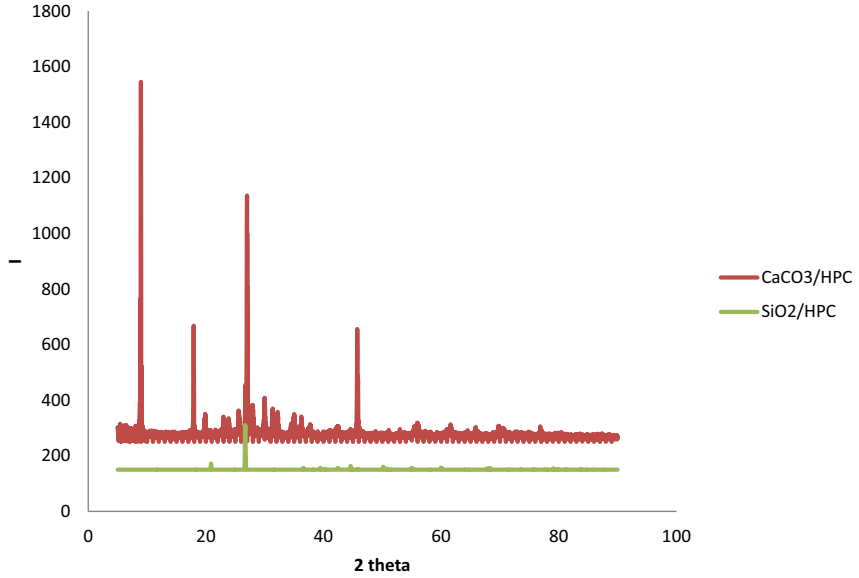

Fig. 4. XRD curves of $CaCO_3$/HPC and $SiO_2/PS/iO_2$ composites.

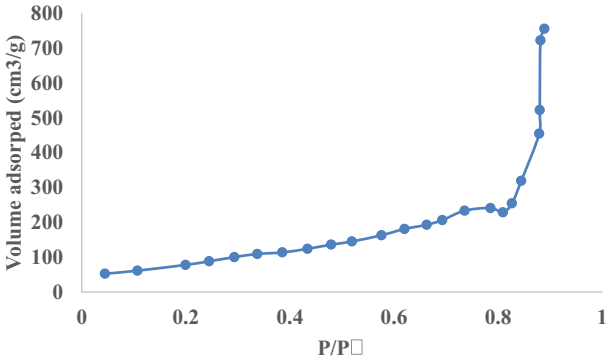

Fig. 5. Nitrogen adsorption and desorption curve of the $CaCO_3$/HPC composite sample.

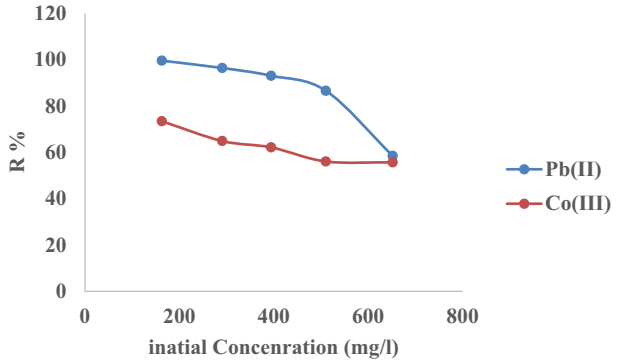

Fig. 7. The concentration effect on the metal ions adsorption by $CaCO_3$/HPC composite.

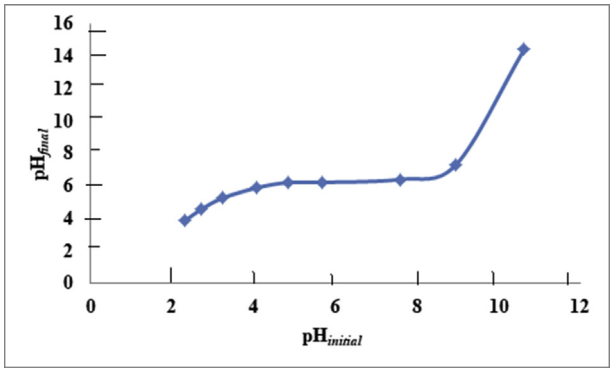

Fig. 6. The pH_{final} as a function of the $pH_{initial}$ for $CaCO_3$/HPC composite.

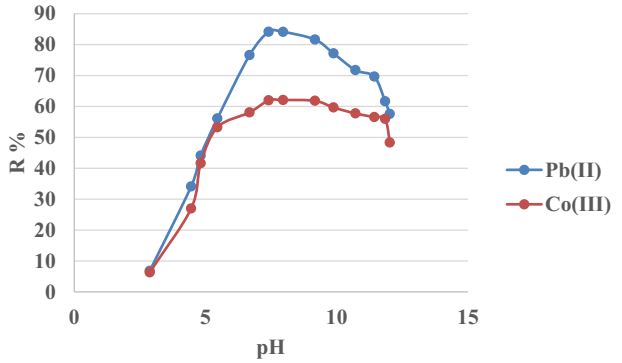

Fig. 8. Adsorption rate of Pb(II) and Co (III) on the CaCO3/HPC composite -pH curve.

a difference was observed near 2θ = 20–40° this resulted from the influence of coexisting phases of amorphous calcium carbonate and crystalline calcium carbonate (Fig. 4). For greater reaction holding process, the identification of amorphous calcium carbonate by wide angle XRD analysis was challenging [34].

The XRD pattern of HPC core shell composite illustrates a sharp peak at a 2Θ value of 26.67° peak corresponding to (002) plane of graphite which has been shifted from 25.89°. This clearly justifies the graphitization of amorphous material into a crystalline material after the leaching process. The shift in the peak to a greater diffraction angle with strident intensity suggests a proliferation of the graphite thickness and diminution in the interlayer spacing of *d* (002) plane. Apart from the graphitic peak, a peak at 54.8° analogous to (004) plane is sharper (as marked in Fig. 4) [35, 36].

3.5. Surface area analysis

Fig. 5 displays the $CaCO_3$/HPC composite N_2 sorption-desorption isotherms.

The prepared sample's N_2 adsorption-desorption isotherms conformed to type IV and had a type H3 hysteresis loop showing the presence of mesopores in this sample (aperture range 2–50 nm). At the same time, we can also calculate the specific nanotubes surface area (BET) where the specific $CaCO_3$/HPC surface area is the largest, approximately 820 m^2/g [37].

3.6. pH of the point of zero charge (pHPZC)

The pH_{PZC} value was 5.5 for $CaCO_3$/HPC composite. As shown in Fig. 6, the pH final is lower than pH initial which implies the acidic character CaCO3/HPC composite adsorbent, and then the surface has a positive charge below pH value of 5.5 [38].

3.7. Effect of initial metal ion concentration

The initial concentration of metal ions in aqueous solutionscontrols the metal adsorption. In the present study, the effects of the initial metal concentrationson the adsorbent $CaCO_3$/HPC composite have been studied in the range100–700 mg/L. Fig. 7 shows that when the initial metal concentration increased, the percentage adsorption of heavy metals decreased.

This could be attributed to the metal particle size (50 μm) used in the experiment, and the lowest adsorption of metals was observed with a high initial concentration of metals. At high concentrations, the competitive dispersion of metal ions has increased at the sites available adsorbent surface; these pores are closed and metal ions are prevented from passing deep into the absorbent pores, which means that adsorption occurs only on the surface [39].

3.8. Effect of solution pH on adsorption of heavy metals

The influence of pH is the main factor influencing the adsorbent acting force on the heavy metal adsorption test. The Pb(II) and Co (III) adsorption rate-pH curve on the $CaCO_3$/HPC composite is shown in Fig. 8.

In this figure, all curves move in the direction of low pH. It can also be seen from the figure that the rate of removal of Pb(II) in $CaCO_3$/HPC composite reaches more than 20% at pH = 4, and the rate of removal of Pb(II) is nearly 85% at pH = 6. The rate of removal of $CaCO_3$/HPC composite at pH = 2 was only 28 percent. The rate of removal at pH = 6 was 85 percent and the rate of removal of Co (III) for $CaCO_3$/HPC composite increased rapidly at pH = 2–5. The rate of removal was almost completely occurred at pH 6. Also the rate of removal of $CaCO_3$/HPC

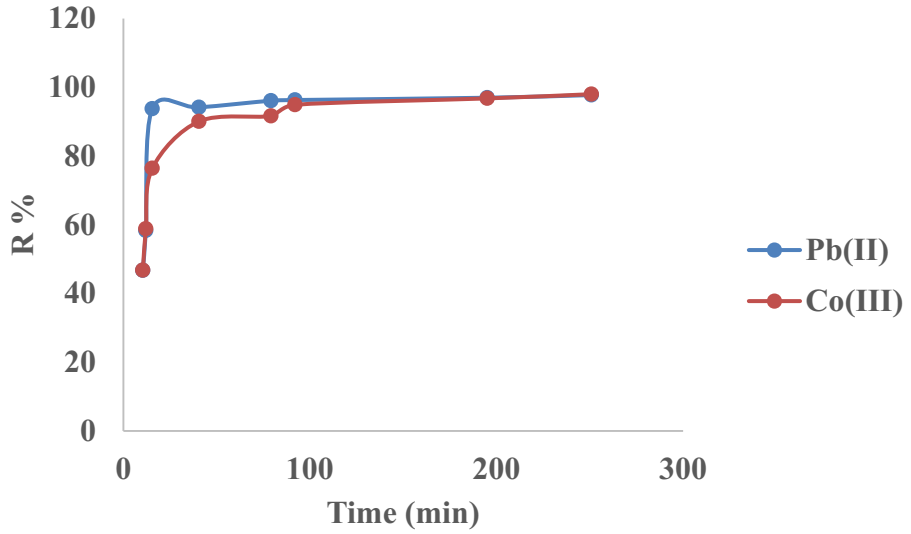

Fig. 9. Kinetics of Adsorption of Heavy Metals on $CaCO_3$/HPC composite.

composite increased slowly with increasing pH, and the rate of removal at pH 7 = 60 %. When the solution pH varies from 2.0 to 4.0, the adsorption efficiency is increased due to the exposure of the heavy metal solution to the negative charges on the diatomite surface????and the strong attraction of the metal ions. The variation in the removal rate of Co (III) with $CaCO_3$/HPC composite during pH changes is non-pronounce [40, 41].

The experimental results show that the rate of removal of the CaCO3/HPC composite increases sharply with the increase in pH for adsorption of Pb(II) and Co(III) and ultimately reaches the same level; where the pH value of the CaCO3/HPC composite is higher when adsorbing lead ions [42].

Also in the higher pH conditions the diatomite particles is slightly unstable as a results of presence of –OH- radical that can be precipitate or dissolve in alkaline condition. So the batch experiments were conducted at pH equal to 6, to keep and preserves the chemical stability of the diatomite. The pH of the solution influence the chemical groups on to the adsorbent surfaces, where the following equations describe the process:

$$M^{2+}+nH_2O \rightarrow M(H_2O)_n^{2+} \quad (3)$$

$$M(H2O)_n^{2+} \rightarrow M(H_2O)_n^{-1} + H^+ \quad (4)$$

$$nM^{2+}+mH_2O \rightarrow M(OH)_m^{(2n-m)}+mH^+ \quad (5)$$

The figure displayed a general trend of increasing heavy metals removal with increasing pH values until maximized at pH = 4. The results indicate that the slow metal uptake shown by $CaCO_3$/HPC composite at low pH values (pH = 2), which can be explained by increasing the positive charge (protons) density on the surface sites and thus, electrostatic repulsion occurred between the heavy metal ions (M^{2+}) and the edge groups with positive charge (C–OH^{2+}) on the surface of $CaCO_3$/HPC composite, which is agreed with by [43].

3.9. Kinetic curve

$CaCO_3$/HPC composite is the best composite adsorbent, according to the experimental study in the previous section; so we will further study their adsorption kinetic performancesin this section. Fig. 9 displays the kinetic curve of $CaCO_3$/HPC composite Pb(II) and Co(III) adsorption.

Adsorption of heavy metal ions from adsorption medium is very fast, basically in a linear trend [44]. $CaCO_3$/HPC composite removal rate of Pb(II) and Co(III) reaches 60% and 40%, respectively, when adsorption time reaches 10 min. The rising trend of the kinetic curve became slower after 10 minutes of adsorption time, and after 120 min the removal rate did not increase substantially, i.e. the adsorption reached equilibrium. The removal rates of Pb(II) and Co(III) were 100 %, and 98 %, respectively, when the adsorption reached equilibrium. It can therefore be seen that $CaCO_3$/HPC composite can remove heavy metal ions completely in a short time [42].

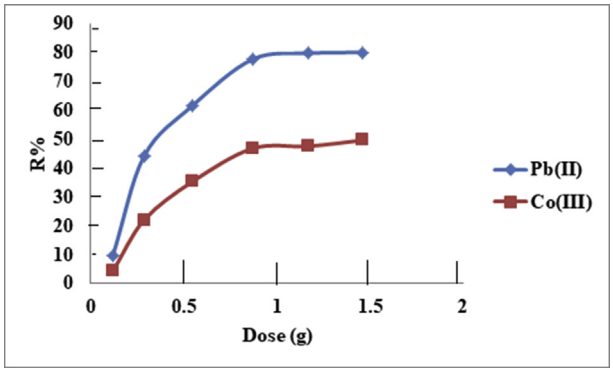

Fig. 10. Effect of $CaCO_3$/HPC composite on Pb(II) and Co(III) adsorption.

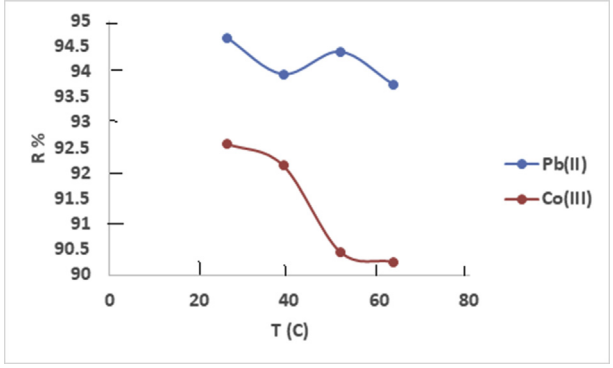

Fig. 11. Efficiency of adsorption versus temperature for analyzed metal ions using model solutions with concentration 100 mg/L (adsorption time 20 min, accuracy ±0.5%).

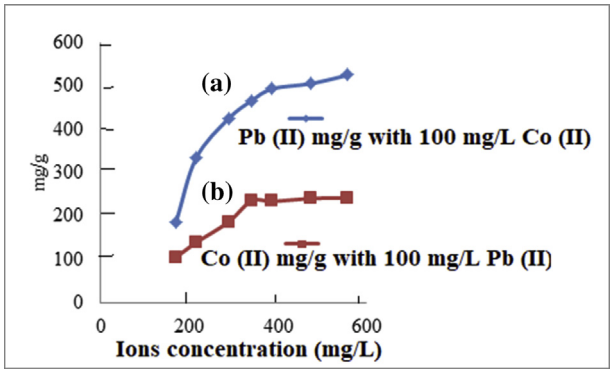

Fig. 12. Adsorption capacity of (a) Pb(II) in single-metal and binary-metals systems and (b) Co(III) in single-metal and binary-metals systems by $CaCO_3$/HPC composite.

3.10. Effect of adsorbent dosage

Adsorbent dosage is an important parameter because of its strong effect on the capacity of the $CaCO_3$/HPC composite at a given initial concentration of the pollutants. The effect of various doses of $CaCO_3$/HPC composite (0.05–1.5 g L^{-1}) on heavy metals removal was studied in the current study at 25 °C (Fig. 10).

The obtained data regarding removal efficiency of heavy metals is increased from 45% to 86.7% by increasing the amount of the adsorbent between 0.5 and 1.5 g L^{-1}, this is because at low $CaCO_3$/HPC composite content, all surface sites are exposed for metal ions and the surface reaches saturation faster, which means that the adsorption of metals had the highest values using 1.5 g $L^{-1}$of the $CaCO_3$/HPC composite, also can be attributed to the availability of larger surface area and the quantity of the adsorption sites [45, 46]. Regarding the data, the removal efficiency was recorded 86.7% for Pb(II) while the lowest value was recorded for Co(III) 40% using 1.5 g L^{-1} of the adsorbent. Therefore, the amount of 1.5 g L^{-1} was selected as the optimum dosage of the used diatomite under study [47] studied the removal of lead ions from wastewater using diatomite. The maximum obtained removal efficiency was 88.09% by using 2 g L^{-1} carbon materials for 20 min, which is close to the results of the current study.

3.11. Effect of temperature on the removal of heavy metals by $CaCO_3$/HPC composite

To study the effect of this parameter on the kinetics of Pb(II) and Co(III)adsorption by $CaCO_3$/HPC composite, we selected the following temperatures: 25, 36, 45 and 65 °C. The results obtained are presented in Fig. 11.

The results obtained indicate that an increase in the temperature in the interval 25–65 °C for the Co(III) solution and for the Pb(II) solution results into a decrease in these metals adsorption capacity which explains an exothermic process, whereas the Pb(II) removal is independent of temperature [48]. We also note that for the metals, the temperature did not influence the equilibrium time. Thus, environmental temperature is an important parameter that can influence the effectiveness of the adsorbent. In general, increasing the temperature weakens the physical or chemical attractive forces and reduces the sorbent ability. For this study, the temperature increase implies a slight decrease in Pb(II) removal rate than Co(III), which proves the efficiency of the $CaCO_3$/HPC composite.

3.12. Adsorption of Pb(II) and Co(III) in binary-metals system on $CaCO_3$/HPC composite

To evaluate the mutual effects of the coexisting Pb(II) and Co(III) on their respective adsorption on the studied $CaCO_3$/HPC composite, the adsorption tests coexisting Pb(II) and Co(III) were performed by varying one metal concentration with another one fixed at 200 mg/L, and the results areshown in Fig. 12.

With the coexistence of Co(III), the Pb(II) adsorption on $CaCO_3$/HPC composite was not affected significantly in comparison with the single-metal system (Fig. 12). The adsorption capacity of Pb(II) at different initial concentrations (200–700 mg/L) almost maintained at the same level as no Cd(II) addition [49]. However, the Co(III) adsorption on $CaCO_3$/HPC composite was seriously inhibited when they coexisted with Pb(II) (Fig. 12). The adsorption capacities of Co(III) by $CaCO_3$/HPC composite in binary-metals system at different initial concentrations were all lower than those in single-metal system and the gap in adsorption capacity between them was growing with the initial concentration of Co(III) increasing. Especially, adsorption capacity for Co(II) in single-metal system at the initial metal concentration of 200 mg/L was 150 mg/g, while it dropped to 100 mg/g in binary-metals system [50]. This difference suggested the competitive adsorption occurred when Pb(II) and Co(III) coexisted in a liquid environment [51]. In comparison with Co(III), the studied $CaCO_3$/HPC composite was favorable to adsorb Pb(II), especially when there were insufficient adsorption sites on $CaCO_3$/HPC composite for all heavy metals. Hence, in binary-metals system with high concentration of heavy metals, the available adsorption sites on $CaCO_3$/HPC composite were occupied by Pb(II) preferentially, resulted in the fact that Co(III) adsorption was inhibited, but the uptake of Pb(II) almost maintained at the same level as single-metal system [52].

Table 1
Lagergren 1st order kinetics analysis results.

Heavy metal ions	Treatment	K_1 (1/min)	R^2 of line fitting
Pb(II)	CaCO3/HPC composite	0.0169	0.8721
Co(III)	$CaCO_3$/HPC composite	0.0222	0.8873

Table 2
Results based on the second order kinetic model analyses.

Heavy metal ions	Treatment	Initial sorption rate (K_2qe^2)	R^2 of line fitting
Pb(II)	$CaCO_3$/HPC composite	2.0619	0.9688
Co(III)	$CaCO_3$/HPC composite	2.4706	0.9857

3.13. Adsorption kinetics

To further understand the adsorption kinetics, all adsorption data were analyzed using the Lagergren 1st order and the pseudo 2nd order models.

Lagergren 1st order kinetics model. This model assumes the adsorption rate (dq_t/dt) and concentration gradient ($q_e - q_t$) follow a first order correlation and can be expressed by Eq. (6):

$$\mathrm{dqtdt} = \mathrm{K1(qe-qt)}\ [53] \tag{6}$$

where q_e is the equilibrium heavy metal adsorption per unit weight of filter (mg/g), q_t is the heavy metal adsorption at any time (t) (min) prior to equilibrium adsorption, and K_1 is the adsorption rate constant (1 min^{-1}).

Applying the boundary condition and initial condition: $q_t = 0$ at $t = 0$, and $q = q_e$ at time t, the above equation can be solved and expressed as: $\ln(q_e - q_t) = \ln q_e - K_1 t$. As a result, plotting $\ln(q_e - q_t)$ versus time (t) will generate a straight line with the slope being $-K_1$ and intercept $\ln q_e$. Using this methodology, we have obtained the corresponding adsorption rate constants for all ions and have listed them in Table 1. From Table 1, one can see $CaCO_3$/HPC composite have higher rate constants (K_1) as compared to the control untreated sample for all heavy metal ions. The relative increase in K_1 over the control for different ions follows the trend of: Pb(II)>Co(III). This result agrees with the Pearson' soft acid–soft base

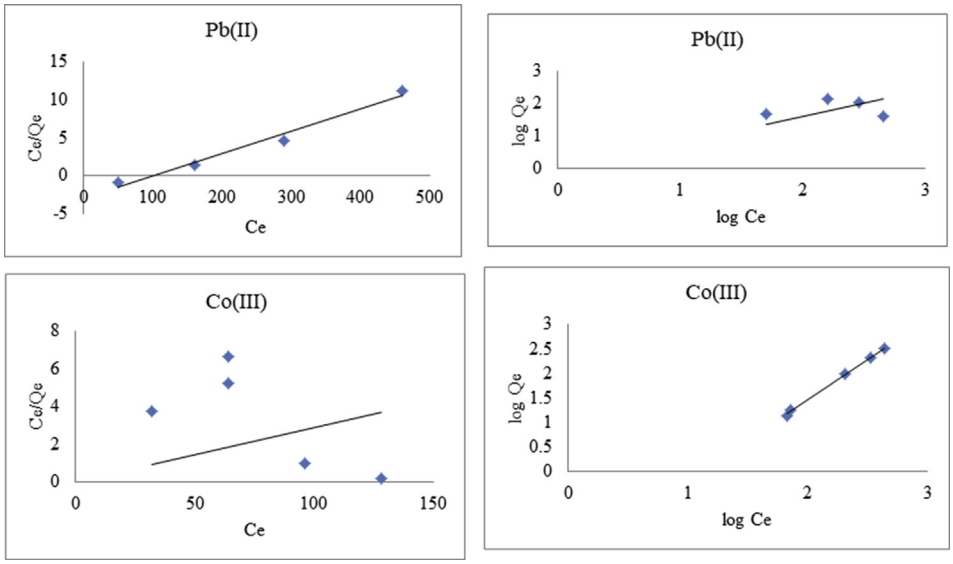

Fig. 13. Langmuir and Freundlich adsorption isothermal model of Pb(II) and Co(III) ions adsorption on $CaCO_3$/HPC composite.

Table 3
Langmiuer and Freundlich adsorption isothermal model parameters for Pb(II) adsorption on $CaCO_3$/HPC composite.

Isotherm equation	$CaCO_3$/HPC core shell composite			
	308	323	343	363
Langmuir				
q 0 (mg g^{-1})	2.046	17.6	38.904	82.987
K (L mg^{-1})	0.0254	0.0867	0.2114	0.5119
R 2	0.9978	0.9303	1	0.9860
R L	0.124	0.258	0.365	0.247
Freundlich				
k f	0.014	0.062	0.0893	1.0521
n	0.8404	0.8258	1	0.5810
R 2	0.0223	0.0572	0.0707	0.4766

predictions as thiol is a soft base ligand and has a high affinity for soft bases such as Hg(II) and Cd(II). The Pb(II) ion on the other hand is a borderline acid, and thus shows the least improvement over control [54].

Pseudo 2nd order model. This model shows the metal ion adsorption rate and adsorption gradient follows the 2nd order correlation (Eq. 7):

$$\mathrm{dqtdt} = \mathrm{K_2(qe-qt)^2}\ [55] \tag{7}$$

After separating of variables and integrating using the initial and boundary conditions ($t = 0$, $q_t = 0$, $t = t$, $q = q_e$), the analytical solution to the above differential equation can be expressed by Eq. (8):

$$\mathrm{tqt} = {}^{1}\mathrm{K_2qe^2}+1\mathrm{qet}\ [56] \tag{8}$$

As a result, a plot of t/q_t vs. t should yield a straight line with the intercept of $1/\mathrm{K_2qe^2}$ where $\mathrm{K_2qe^2}$ represents the initial sorption rate. Results for these are listed in Table 2.

From Table 2, the initial sorption rate (K2qe2) improvement over control follows the order of: Pb(II) > Co(III). This result once again suggests Hg^{2+} has the fastest initial adsorption rate among all ions. Based on both the 1st order and 2nd order kinetics analyses, it is clear that the introduction of $CaCO_3$/HPC composite has greatly enhanced the removal rate of all target heavy metal ions with Pb(II) being the most effective ion to be removed. These results are consistent with the high reactivity of Pb(II) toward the $CaCO_3$/HPC composite due to the precipitation reaction on the core. A similar finding has also been reported by Saha et al. [57].

3.14. Isothermal studies

In order to examine the fundamental adsorption properties regarding interaction and capacity, equilibrium measurements were performed. The Langmuir (Eq. 9) and Freundlich (Eq. 10) models were used to fit the experimental data.

Table 4
Langmiuer and Freundlich adsorption isothermal model parameters for Co(III) adsorption on $CaCO_3$/HPC composite.

Isotherm equation	SWPS			
	308	323	343	363
Langmuir				
q 0 (mg g^{-1})	0.4576	3.468	2.0041	1.585
K (L mg^{-1})	0.0130	0.018	0.0046	0.005
R 2	0.7725	0.9579	0.9612	0.855
R L	0.4336	0.4397	0.6832	0.683
Freundlich				
k f	1.6552	0.1835	0.3832	0.0126
n	0.8531	0.6383	0.8621	0.7828
R 2	0.999	0.9986	0.8952	0.983

$$q = {}_{\mathrm{qmKLCe}}/(1 + Ce) \tag{9}$$

$$q = KFC1/ne \tag{10}$$

where q is the amount of Pb(II) and Co(III) adsorbed on $CaCO_3$/HPC composite in different concentrations; qm is the saturated adsorption capacity; KL is a constant of the Langmuir isotherm; Ce is the equilibrium Pb(II) and Co(III) concentration remaining in solution; KF is the Freundlich constant (L mg^{-1}), which indicates the relative adsorption capacity of the adsorbent; n is the heterogeneity factor and is known as Freundlich coefficient. The fitting results are shown in Fig. 13.

Table 3 shows Langmuir and Freundlich adsorption isothermal model parameters for Pb(II) adsorption on $CaCO_3$/HPC composite.

These results showthat the maximum removal capacities of Pb(II) were in the following order: $CaCO_3$/HPC compositewith an $CaCO_3$ core, indicating that the active sites and adsorption capacity were enhanced with the modification [58]. However, the primitive effect did not change regularly with the increase in $CaCO_3$/HPC composite. Correlation coefficients showed that the Langmuir model fitted the Pb(II) adsorption data better than the Freundlich model, implying a monolayer adsorption trend. As for the Co(III) adsorption, it was promoted from 27.4 mg g^{-1} to 57.60 mg g^{-1} with an increasing $CaCO_3$/HPC composite. This tendency illustrated well the feasibility $CaCO_3$/HPC compositemodification in synthesis. The Freundlich constant (KF) for Co(III) adsorption with an $CaCO_3$/HPC composite (Table 4), much higher than for others, which

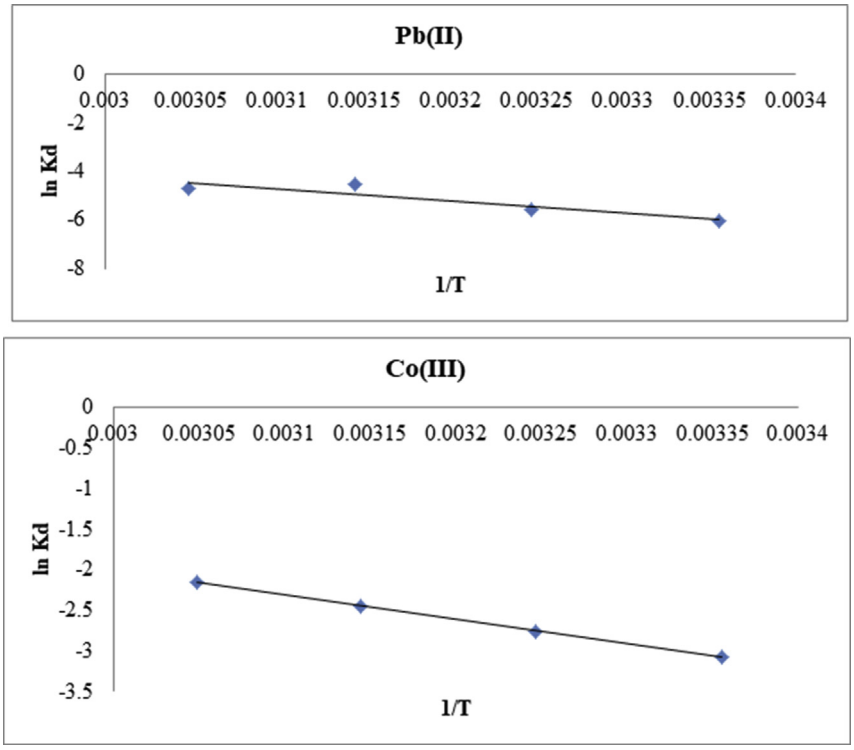

Fig. 14. Fitting curve of adsorption process for Pb(II) and Co(III).

Table 5
Thermodynamic parameters of adsorption process for Pb(II).

T	ΔS	ΔH	Δ G
298	90.6772	41912.1	−15.034
308			−14.254
318			−12.008
333			−12.826

Table 6
Thermodynamic parameters of adsorption process for Co(III).

T	ΔS	ΔH	Δ G
298	60.6772	476.1	−15.43
308			−14.44
318			−13.18
333			−12.546

indicates the potential of adsorption. The value of $1/n$ for both Pb(II) and Co(III) lies between 0 and 1 further confirming the favorable adsorption for both metals.

3.15. Thermodynamic studies

The temperature has substantial effect on Pb(II) and Co(III) adsorption degree of the $CaCO_3$/HPC, and the summarized results are shown in Fig. 14.

It can be seen that the equilibrium adsorption capacity decreases from 200 to 450 mg g^{-1} with temperature increasing from 298 to 333 K. The effect of the temperature on the adsorption behavior is determined by the thermodynamic properties of Re adsorption, and the thermodynamic parameters such as Gibbs free energy change (ΔG), enthalpy change (ΔH) and entropy change (ΔS) for the adsorption system can be calculated using the following Eqs. (11) and (12):

$$\Delta G^{\circ} = -_{RTlnKd} \quad (11)$$

$$\ln Kd = \Delta S^{\circ}/R - \Delta H^{\circ}/R \times 1/T \text{ [59]} \quad (12)$$

where R is the gas constant (8.314 J mol^{-1} K^{-1}), T is the absolute temperature (K), Kd is adsorption equilibrium constant and Ca is the concentration of Pb(II) and Co(III) on the adsorbent at the equilibrium (mg·L^{-1}). The curve between lnKd and $1/T$ is drawn in Fig. 14, in which the fitted straight slope represents $\Delta H/R$ and the intercept is $\Delta S^{\circ}/R$. The calculated thermodynamic parameters are shown in Tables 5 and 6.

It could be observed that the value of ΔG° increases from −15.034 to −12.826 kJ $mol^{-1}$and from 15.4 to 12.5 with temperature increasing from 298 to 333 K for Pb(II) and Co(III) respectively, indicating that the adsorption reaction of Pb(II) and Co(III) on the $CaCO_3$/HPC is a spontaneous process. Moreover, the variation of the Gibbs free energy verifies that the degree of the spontaneous reaction for Pb(II) and Co(III) adsorption is much stronger at lower temperature [60].

4. Conclusion

In this study, a new $CaCO_3$/HPC compositeadsorbent was prepared for adsorption of Pb(II) and Co(III) ions from aqueous solutions by the co-precipitation process. BET analysis showed that the surface area were 800 m^2 g^{-1}, respectively. XRD pattern of $CaCO_3$/HPC compositeshowed a low crystallinity. The effect of parameters such as pH, contact time and temperature was investigated on the adsorption of Pb(II) and Co(III) from aqueous solutions. Three isotherm models, namely Langmuir and Freundlich were used for analysis of equilibrium data. The results showed that the Langmuir isotherm described the equilibrium data of Pb(II) adsorption better than the other isotherm models and Freundlich for Co(III) representing that the adsorption was monolayer and maximum adsorption capacities for Pb(II), at the temperature of 45°C. The adsorption capacity of U(VI) and Th(IV) ions by the $CaCO_3$/HPC compositewas in the order of Pb(II) > Co(III). The adsorption kinetic studies of both metal ions explained that the experimental data were best described by pseudo second order indication chemo sorption adsorption mechanism. The positive values of the enthalpy changes showed that

Pb(II) and Co(III) adsorption processes were endothermic. Negative values of Gibbs free energy changes showed that the adsorption of these metal ions onto the $CaCO_3$/HPC compositeadsorbent was spontaneous. The results of inhibitory effect of ions on the Pb(II) and Co(III) adsorption onto the Pb(II) and Co(III) showed that the adsorption capacity of Pb(II) and Co(III) ions decreased in binary systems, according to the descending order of Pb(II) > Co(III), respectively.

Declarations

Author contribution statement

Mahmoud Fathy: Conceived and designed the experiments; Performed the experiments; Wrote the paper.

Mohamed A. Zayed: Analyzed and interpreted the data; Wrote the paper.

Y. M Moustafa: Analyzed and interpreted the data; Contributed reagents, materials, analysis tools or data; Wrote the paper.

Funding statement

This work was supported by the Egyptian Petroleum Research Institute (EPRI), Egypt.

Competing interest statement

The authors declare no conflict of interest.

Additional information

No additional information is available for this paper.

Acknowledgements

The authors are thankful to the Central Instrumentation Facility Centre (CIFC) for providing the instrumental facilities.

References

[1] R. Cai, et al., Metal-free core-shell structured N-doped carbon/carbon heterojunction for efficient CO2 capture, Carbon 150 (2019) 43–51.
[2] N. Pamphile, et al., Synthesis of a novel core-shell-structure activated carbon material and its application in sulfamethoxazole adsorption, J. Hazard Mater. 368 (2019) 602–612.
[3] G.D. Cai, et al., Toughening polystyrene by core–shell grafting copolymer polybutadiene-graft-polystyrene with potassium persulfate as initiator, J. Ind. Eng. Chem. 19 (3) (2013) 823–828.
[4] S. Li, et al., High-efficiency enhancement on thermal and electrical properties of epoxy nanocomposites with core-shell carbon foam template-coated graphene, Compos. Appl. Sci. Manuf. 120 (2019) 95–105.
[5] W. Su, et al., NiCo-LDH nanowires@nanosheets core-shell structure grown on carbon fiber cloth for high performance flexible supercapacitor electrode, J. Alloy. Comp. 799 (2019) 15–25.
[6] Z. Mokadem, et al., Triazole containing magnetic core-silica shell nanoparticles for Pb2+, Cu2+ and Zn2+ removal, Ar. J. Chem. 10 (8) (2017) 1039–1051.
[7] A.K. Dhawan, J.W. Seyler, B.C. Bohrer, Preparation of a core-double shell chitosan-graphene oxide composite and investigation of Pb (II) absorption, Heliyon 5 (1) (2019), e01177.
[8] F. Wang, et al., Core-shell FeCo@carbon nanoparticles encapsulated in polydopamine-derived carbon nanocages for efficient microwave absorption, Carbon 145 (2019) 701–711.
[9] K. Zhou, et al., Constructing hierarchical polymer@MoS2 core-shell structures for regulating thermal and fire safety properties of polystyrene nanocomposites, Compos. Appl. Sci. Manuf. 107 (2018) 144–154.
[10] Z. Wang, et al., Optical absorption of carbon-gold core-shell nanoparticles, J. Quant. Spectrosc. Radiat. Transf. 205 (2018) 291–298.
[11] C. Jiang, et al., Construction of magnetic lignin-based adsorbent and its adsorption properties for dyes, J. Hazard Mater. 369 (2019) 50–61.
[12] X. Wang, et al., Ultrasonic method to synthesize glucan-g-poly(acrylic acid)/sodium lignosulfonate hydrogels and studies of their adsorption of Cu2+ from aqueous solution, ACS Sustain. Chem. Eng. 5 (8) (2017) 6438–6446.
[13] Y. Wang, et al., Synthesis of aminated calcium lignosulfonate and its adsorption properties for azo dyes, J. Ind. Eng. Chem. 61 (2018) 321–330.
[14] X. Wang, et al., Carbon composite lignin-based adsorbents for the adsorption of dyes, Chemosphere 206 (2018) 587–596.
[15] P. Komar, et al., Core-shell spheroidal microparticles with polystyrene cores and rich in polyglycidol shells, Polymer 146 (2018) 6–11.
[16] S. Feng, et al., A general approach for encapsulating nanoparticles by polystyrene-block-poly(acrylic acid) shell in colloidal, J. Phys. Chem. Solids (2019).
[17] D. Sarma, et al., TSEM-based contour analysis as a tool for the quantification of the profile roughness of silica shells on polystyrene core particles, Appl. Surf. Sci. 426 (2017) 446–455.
[18] U. Patil, et al., Ultrasound-assisted improvements in biocatalytic activity and production of organic-solvent stable protease from Bacillus circulans MTCC 7942, Ultrason. Sonochem. 40 (2018) 201–205.
[19] H.-S. Kong, B.-J. Kim, K.-S. Kang, Synthesis of CaCO3–SiO2 composite using CO2 for fire retardant, Mater. Lett. 238 (2019) 278–280.
[20] X. Zuo, et al., Desalination of water with a high degree of mineralization using SiO2/PVDF membranes, Desalination 311 (2013) 150–155.
[21] Mahmoud Fathy, T. A.M., Ahmed Elsayed Awad Allah, A.-H.A.-A. El-Bellihi, Preparation of cation-exchange resin from styrene-divinylbenzene copolymer obtained by suspension polymerization method, Elixir Int. J. (2014).
[22] M. Ramzi, et al., Breakthrough Curves of Oil Adsorption on Novel Amorphous Carbon Thin Fi Lm, 2016.
[23] E. Neofotistou, K.D. Demadis, Use of antiscalants for mitigation of silica (SiO2) fouling and deposition: fundamentals and applications in desalination systems, Desalination 167 (2004) 257–272.
[24] Y. Yue, J.J. Wang, Y. Bai, Tracing the status of silica fume in cementitious materials with Raman microscope, Constr. Build. Mater. 159 (2018) 610–616.
[25] J. Meng, et al., Facile fabrication of 3D SiO2@Graphene aerogel composites as anode material for lithium ion batteries, Electrochim. Acta 176 (2015) 1001–1009.
[26] M. Vetter, et al., The use of Raman spectroscopy to monitor phase changes in concrete following high temperature exposure, Constr. Build. Mater. 204 (2019) 450–457.
[27] G. Amini, S.N. Banitaba, A.A. Gharehaghaji, Imparting strength into nanofiberous yarn by adhesive bonding, Int. J. Adhesion Adhes. 75 (2017) 96–100.
[28] D.M. Chipara, et al., Raman spectroscopy of polystyrene nanofibers—multiwalled carbon nanotubes composites, Appl. Surf. Sci. 275 (2013) 23–27.
[29] W. Cheng, Preparation and properties of lignocellulosic fiber/CaCO3/thermoplastic starch composites, Carbohydr. Polym. 211 (2019) 204–208.
[30] Y. Zhang, et al., Synthesis of novel graphene oxide/pristine graphene/polyaniline ternary composites and application to supercapacitor, Chem. Eng. J. 288 (2016) 689–700.
[31] D. Chen, et al., Removal of methylene blue and mechanism on magnetic γ-Fe2O3/SiO2 nanocomposite from aqueous solution, Water Resour. Ind. 15 (2016) 1–13.
[32] T.H.T. Vu, et al., Solvothermal synthesis of Pt -SiO2/graphene nanocomposites as efficient electrocatalyst for methanol oxidation, Electrochim. Acta 161 (2015) 335–342.
[33] Y. Han, et al., Effect of alternating electromagnetic field and ultrasonic on CaCO3 scale inhibitive performance of EDTMPS, J. Taiwan Inst. Chem. Eng. 99 (2019) 104–112.
[34] Y. Fu, et al., Investigation on enhancing effects of Au nanoparticles on solar steam generation in graphene oxide nanofluids, Appl. Therm. Eng. 114 (2017) 961–968.
[35] M.J. I, et al., Augmentation of graphite purity from mineral resources and enhancing % graphitization using microwave irradiation: XRD and Raman studies, Diam. Relat. Mater. 88 (2018) 129–136.
[36] Y. Zhu, et al., 3D graphene frameworks with uniformly dispersed CuS as an efficient catalytic electrode for quantum dot-sensitized solar cells, Electrochim. Acta 208 (2016) 288–295.
[37] Mahmoud Fathy, T. A.M., Ahmed E. Awadallah, A.-H.A.-A. El-Bellihi, Adsorption kinetics of sulfates by anion exchange resin containing pristine multiwalled carbon nano tubes, Glob. J. Res. Eng.: C. Chem. Eng. 1 (14) (2014).
[38] Y. Abdellaoui, et al., Comparison of the divalent heavy metals (Pb, Cu and Cd) adsorption behavior by montmorillonite-KSF and their calcium- and sodium-forms, Superlattice Microstruct. 127 (2019) 165–175.
[39] G.M. Al-Senani, F.F. Al-Fawzan, Adsorption study of heavy metal ions from aqueous solution by nanoparticle of wild herbs, Egypt. J. Aquatic Res. 44 (3) (2018) 187–194.
[40] M. El-Sayed, M.R.R. Hosny, M. Fathy, Th. Abdel Moghny, Breakthrough curves of oil adsorption on novel amorphous carbon thin film, Water Sci. Technol. 73 (10) (2016) 2361–2369.
[41] Abd El Hay Ali Farrag, T. A.M., Atef Mohamed Gad Mohamed, Saleem Sayed Saleem, Mahmoud Fathy, Abu Zenima synthetic zeolite for removing iron and manganese from Assiut governorate groundwater, Egypt, Appl. Water Sci. (2016).
[42] Y. Fu, X. Liu, G. Chen, Adsorption of heavy metal sewage on nano-materials such as titanate/TiO2 added lignin, Result. Phys. 12 (2019) 405–411.
[43] E.E. ElSayed, Natural diatomite as an effective adsorbent for heavy metals in water and wastewater treatment (a batch study), Water Sci. 32 (1) (2018) 32–43.
[44] M. Trgo, et al., Competitive removal of lead(II) and zinc(II) from a binary aqueous solution on a fixed bed of natural zeolite, in: P.M. Antoine Gédéon, B. Florence (Eds.), Studies in Surface Science and Catalysis, Elsevier, 2008, pp. 509–512.
[45] Y.-L. Xie, et al., Graphene/CeO2 hybrid materials for the simultaneous electrochemical detection of cadmium(II), lead(II), copper(II), and mercury(II), J. Electroanal. Chem. 757 (2015) 235–242.

[46] Y. Wang, et al., The removal of lead ions from aqueous solution by using magnetic hydroxypropyl chitosan/oxidized multiwalled carbon nanotubes composites, J. Colloid Interface Sci. 451 (2015) 7–14.
[47] R.L. Campbell, A.T. Jones, Appropriate disposal of effluent from coastal desalination facilities, Desalination 182 (1–3) (2005) 365–372.
[48] M.J. Pirouz, M.H. Beyki, F. Shemirani, Anhydride functionalised calcium ferrite nanoparticles: a new selective magnetic material for enrichment of lead ions from water and food samples, Food Chem. 170 (2015) 131–137.
[49] K.C. Lai, et al., Environmental application of three-dimensional graphene materials as adsorbents for dyes and heavy metals: review on ice-templating method and adsorption mechanisms, J. Environ. Sci. 79 (2019) 174–199.
[50] W.M. Ye, et al., Adsorption, desorption and competitive adsorption of heavy metal ions from aqueous solution onto GMZ01 bentonite, in: Engineering Geology for Society and Territory, ume 6, Springer International Publishing, Cham, 2015.
[51] M. Hossein Beyki, H. Alijani, Y. Fazli, Poly o-phenylenediamine–MgAl@CaFe2O4 nanohybrid for effective removing of lead(II), chromium(III) and anionic azo dye, Process Saf. Environ. Prot. 102 (2016) 687–699.
[52] B.-J. Ni, et al., Competitive adsorption of heavy metals in aqueous solution onto biochar derived from anaerobically digested sludge, Chemosphere 219 (2019) 351–357.
[53] Y. Zhou, O.G. Apul, T. Karanfil, Adsorption of halogenated aliphatic contaminants by graphene nanomaterials, Water Res. 79 (2015) 57–67.
[54] A. Asfaram, et al., Synthesis of magnetic γ-Fe2O3-based nanomaterial for ultrasonic assisted dyes adsorption: modeling and optimization, Ultrason. Sonochem. 32 (2016) 418–431.
[55] J.A. Arcibar-Orozco, D.A. Giannakoudakis, T.J. Bandosz, Effect of Ag containing (nano)particles on reactive adsorption of mustard gas surrogate on iron oxyhydroxide/graphite oxide composites under visible light irradiation, Chem. Eng. J. 303 (2016) 123–136.
[56] N.H. Abdullah, et al., Solid matrices for fabrication of magnetic iron oxide nanocomposites: synthesis, properties, and application for the adsorption of heavy metal ions and dyes, Compos. B Eng. 162 (2019) 538–568.
[57] Z. Xia, et al., Heavy metal ion removal by thiol functionalized aluminum oxide hydroxide nanowhiskers, Appl. Surf. Sci. 416 (2017) 565–573.
[58] K. Shams, S. Najari, Dynamics of intraparticle desorption and chemical reaction in fixed-beds using inert core spherical particles, Chem. Eng. J. 172 (1) (2011) 500–506.
[59] A.M. Soliman, et al., Removal of Pb(II) ions from aqueous solutions by sulphuric acid-treated palm tree leaves, J. Taiwan Inst. Chem. Eng. (2016).
[60] D. Caputo, et al., Fixed-bed ion-exchange process performance of Pb2 + removal from a simulated ceramic wastewater by Neapolitan yellow tuff, in: C.C.A. Gamba, S. Coluccia (Eds.), Studies in Surface Science and Catalysis, Elsevier, 2001, pp. 111–119.